Nonlinear Dyn (2025) 113:20747–20766
https://doi.org/10.1007/s11071-025-11289-8

RESEARCH

An efficient numerical tool for 1-dof nonlinear systems towards large-scale seismic structural health monitoring of masonry buildings

A. Casalotti · F. Milicchio · F. D'Annibale · G. Formica

Received: 23 December 2024 / Accepted: 22 April 2025 / Published online: 28 May 2025

Abstract A nonlinear constitutive model, combined with an ad-hoc developed numerical strategy, is proposed to study the nonlinear dynamics of masonry buildings approached through single degree-of-freedom systems (1-dof). This proposal is explicitly aimed at providing enhancements in designing tools for seismic structural health monitoring in large-scale urban contexts. The model incorporates plasticity and damage induced by friction and wear, and it is capable of capturing the nonlinear response of structures subject to general external time-dependent loads. A numerical algorithm to solve the ensuing piecewise nonlinear equations is devised and explicitly implemented in a low-level language, thus being optimized for specific hardware systems for structural health monitoring. The proposed formulation is initially tested to validate the model's constitutive parameters by identifying them in pseudo-static regimes, according to the experimental behavior of a real-scale single-storey masonry building. Then, the numerical stability of the proposed code is examined in comparison with traditional numerical solvers. Finally, the effects of real seismic actions are investigated, with particular emphasis on the accumulated damage when subsequent quakes are considered.

Keywords Nonlinear dynamics · Masonry buildings · Damage · Friction · Plasticity

A. Casalotti (✉) · G. Formica
Dept. of Architecture, Roma Tre University, 00184 Rome, Italy
e-mail: arnaldo.casalotti@uniroma3.it

F. Milicchio
Dept. of Civil, Computer Science and Aeronautical Technologies Engineering, Roma Tre University, 00146 Rome, Italy

F. D'Annibale
Dept. of Civil, Construction-Architectural and Environmental Engineering, University of L'Aquila, 67100 L'Aquila, Italy

1 Introduction

Seismic structural health monitoring (SHM) provides a comprehensive framework for evaluating the structural integrity and performance of civil infrastructures, utilizing data collected from sensors during routine operations and under extreme conditions [1–3]. Specifically, for masonry buildings and in broader applications, SHM tools not only assess seismic vulnerability but also enable real-time monitoring of building response, optimization of retrofitting strategies, and enhancement of overall resilience to seismic hazards [4,5]. Recent seismic events have highlighted the importance of addressing this emerging research challenge, especially in Italy, where the structural vulnerabilities of old historic centers reveal significant seismic resilience deficiencies [6–8]. Typically, these small towns, characterized by poorly constructed masonry buildings, are located in medium to high seismic hazard zones, such as those of the Alpine and Apennine chains. Mitigating this seismic risk is crucial for preserving the structural, cultural, and functional integrity of these historical areas.

There is indeed a growing demand for streamlined methodologies to assess the seismic vulnerability of groups of masonry buildings on a large scale. This is essential for equipping municipalities with effective management tools, particularly in the pre-earthquake prevention phase, to guide retrofitting efforts, as well as identifying the most vulnerable building clusters for a more rational allocation of aid resources during the post-earthquake emergency response phase (to cite a few recent contributions, see [9–12]).

In the context of large-scale urban monitoring, the development of 1-degree-of-freedom (1-dof) nonlinear models, alongside ad-hoc low-level software codes and hardware systems, is crucial [13]. These models and systems efficiently process sensor data, perform analysis algorithms, and relay results within the specific hardware constraints of the monitoring system. This approach is particularly suited for real-time monitoring applications where timely and accurate detection of structural issues is necessary [14].

Within this framework, simplified models for masonry buildings are developed as equivalent nonlinear 1-dof systems, which directly provide structural capacity curves (resulting shear-force versus tip-displacement). These systems are definitely described by constitutive laws incorporating both stiffness and strength deterioration. Among the most popular, there are hysteretic models [15] or, in general, elasto-plastic models incorporating both hardening and softening responses—see, for instance, [16,17] for a recent review on this topic. It is worth mentioning that international technical standards typically adopt equivalent 1-dof models for design purposes (*e.g.*, ATC-40 [18], FEMA-273 [19]), as well as in Italy, see NTC 2018 [20]. In particular, the friction-driven response along with damage processes plays a key role in the global behavior of masonry buildings, as proved either by experimental tests [21–25] and by enhanced numerical modelings [26–28]. Such a behavior is the result of complex nonlinear phenomena taking place at the interfaces localized in single failure parts of the walls or, in general, on large failure surfaces, leading to a base-shear resulting response under seismic excitations which allows to validate the afore mentioned 1-dof models.

Recent works in the field of interface models have delved into the complexities of friction, wear, and stick-slip phenomena occurring at the interface between different materials [29–33]. This area, situated within Mechanical Sciences, addresses a wide array of applications, ranging from seismic analysis to historical building conservation, friction in medical devices, and more [34–37]. The exploration of non-smooth laws in dynamic problems introduces complex scenarios that require enhanced methodological attention [38–41]. A critical factor in these analyses is a thorough understanding and modeling of interface phenomena, such as friction and abrasion, necessitating sophisticated constitutive models to accurately depict the time evolution of the contact interface and its resultant strong nonlinear behaviors [42].

Particularly, wear—defined as the degradation of the force opposing motion between in-contact bodies—is scrutinized, especially when resulting from abrasion due to stick-slip phenomena [43,44]. The mathematical modeling of these contact phenomena is framed within the Thermodynamics of Irreversible Processes and Damage Mechanics, yielding a comprehensive insight into interfacial phenomena [45–47]. Although much of the research on sliding and friction has focused on quasi-static conditions, there's an increasing necessity to explore their effects in dynamic regimes. Initial studies on the nonlinear dynamics of oscillators utilized bilinear constitutive laws and experimental approaches [48–50]. Moreover, elasto-plastic oscillators, discrete systems exhibiting hysteresis, and systems accounting for damage have also been considered [51–54].

As highlighted in various structural health monitoring contexts, such as [55,56], and specifically in [57] within the domain of cultural heritage preservation, it is crucial to develop ad hoc algorithms explicitly implemented in low-level programming languages. This approach allows optimization for specific hardware systems used in SHM applications. On the other hand, although numerous numerical schemes have been developed over the years to accurately reproduce the behavior of elastoplastic materials in computational environments for solving engineering problems, the numerical solution of such problems remains non-trivial. It requires careful analysis to ensure algorithm robustness, accuracy, and convergence within a reasonable computational time [58].

In particular, within the framework of macroscopic phenomenological modeling, approaches based on theories with internal variables, which describe rate-independent material responses, offer several advantages for engineering simulations. These include modeling simplicity, easier numerical implementation, and reduced computational costs compared to other approaches

(*e.g.*, microscopic models). In rate-dependent contexts-such as the one addressed in the present paper-the regularization of the material response through appropriate algorithms, capable of maintaining computational costs under control while ensuring adequate robustness, becomes even more challenging [59,60].

Contribution

In this paper, we propose a numerical strategy for both fast and robust simulations of the nonlinear dynamic behavior of masonry buildings under dynamic loads, by formulating a reduced-order model coupled with an efficient numerical approach developed for implementation in low-level programming languages.

The proposed 1-dof model is specifically designed to capture the global nonlinear behavior of masonry buildings, incorporating a nonlinear constitutive law that accounts for friction and wear phenomena. This constitutive law is reformulated within a strain-driven framework, a strategy successfully applied in various contexts (see, e.g., [60–62]). This reformulation enables the use of an incremental numerical scheme that avoids iterative procedures to achieve convergence, thereby reducing overall computational time. Specifically, the nonlinear response is integrated within a Runge-Kutta method, which demonstrates competitive performance when expressly tailored for elastoplastic constitutive laws, particularly when embedded within systems of differential-algebraic equations, offering higher-order accuracy and superior stability properties [58].

Moreover, we tailor here the model response to be adapt for simulating the nonlinear structural response of masonry structures as a single degree-of-freedom system (1-dof). To this purpose, the identification of constitutive parameters based on real-world case studies demonstrates the applicability of the 1-dof system in representing real buildings, facilitating their monitoring and assessment.

Finally, we emphasize how the proposed numerical scheme is expressly developed as a `C++` library, which can be compiled and utilized on all compatible hardware, from desktops to microcontrollers such as Arduino or Intel Galileo. By relying solely on portable `C++`, the implemented code runs without limitations, except those due to the specific chosen hardware (*e.g.*, RAM availability). The code is freely and publicly available at https://zenodo.org/records/10808423.

Although an explicit structural health monitoring simulation is not presented in the paper, the numerical investigations here conducted are aimed to be pivotal for innovative methodological approaches, offering an open source software based on an *ad hoc* mechanical formulation aiming at fast computations, and then optimized for specific hardware commonly used in monitoring applications. As part of future developments, we intend indeed to investigate the intrinsic vulnerability of entire building aggregates to seismic events. In this perspective, the preliminary investigations we here provide, covering a wide spectrum of simulations, are considered to be crucial for pursuing such goals.

Outline

The paper is organized as follows. In Sec. 2, the 1-dof model is introduced. Sec. 3 details its numerical formulation and the ensuing algorithm. All the numerical tests are compiled in Sec. 4: the model is initially validated by identifying the constitutive parameters that resemble the experimental behavior of a real-scale single-storey masonry building; the numerical stability of the proposed code, in both static and dynamic regimes, is demonstrated through comparison with standard numerical solvers; finally, the effects of real seismic actions are examined, with particular emphasis on the accumulated damage when subsequent quakes are considered. Some concluding remarks are offered in Sec. 5.

2 A nonlinear 1-dof model for masonry buildings

As described in the Introduction, we here present the 1-dof system adopted to simulate the nonlinear structural response of masonry structures. In particular, we take as reference a single-storey masonry building that has already been the subject of several experimental and numerical investigations [63]. The benchmark structure has an overall height of 4.42 m and is characterized by plan dimensions 4.115×3.905 m^2, built with 0.228 m thick walls, with multiple openings as door and windows. The roof is composed by a 0.152 m thick reinforced concrete slab. A schematic representation of the structure is given in Fig. 1; for a complete geometric and mechanical details please refer to [63].

2.1 Constitutive model description

The 1-dof reduced order model is schematically represented in Fig. 2 as an interface model. The stress at the interface, namely τ, evolves in time according to the law:

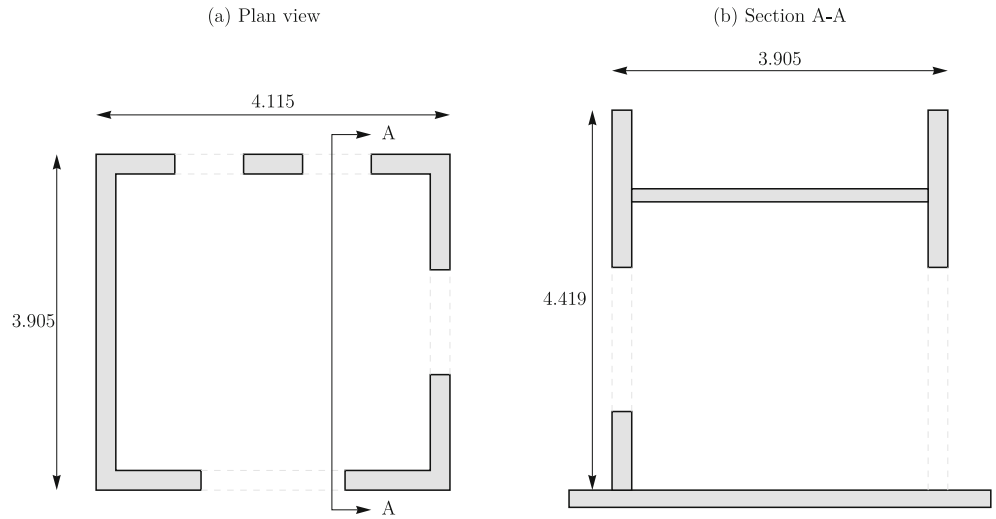

Fig. 1 Plan view (a) and vertical cross section (b) of the one-storey masonry building taken as reference. For further details, see [63]

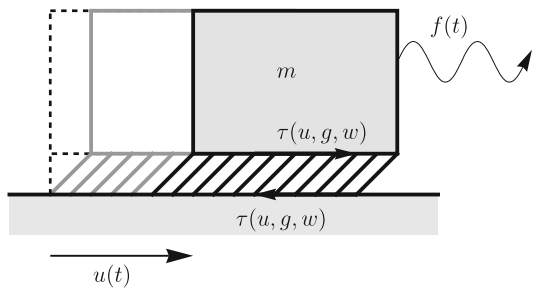

Fig. 2 Schematic representation of the 1-dof model

$$\dot{\tau} = k_a(1-w)(\dot{u}-\dot{g}) - k_a\dot{w}(u-g)\,. \tag{1}$$

Denoting with g, α, w the internal variables associated to the inelastic displacement, hardening and wear, respectively, their evolution is governed by the following rate equations:

$$\begin{aligned}
\dot{g} &= \mathrm{s_w}\frac{H}{(1-w)^2}\dot{\tau}\,,\\
\dot{\alpha} &= \mathrm{s_w}\frac{H}{1-w}\mathrm{sign}(\tau)\dot{\tau}\,,\\
\dot{w} &= \mathrm{s_w}\frac{H}{(1-w)}\left(\frac{W}{\Gamma}\right)^{\gamma}\mathrm{sign}(\tau)\dot{\tau}\,,
\end{aligned} \tag{2}$$

where H represents the so-called hardening function, while A and W are the forces thermodynamically associated to α and w, respectively, according to the expressions reported below:

$$\begin{aligned}
H = \Bigg\{ & a\left(A_\infty - \frac{A}{1-w}\right)\\
& + \left[A_\infty - 2A_\infty(1-w+\frac{a}{2}\alpha)e^{-\frac{a}{1-w}\alpha} + \frac{||\tau||}{(1-w)^2}\right]\\
& \left(\frac{W}{\Gamma}\right)^{\gamma}\Bigg\}^{-1}, \quad A = A_\infty(1-w)\left[1-(1-w)e^{-\frac{a}{1-w}\alpha}\right],\\
W = & \frac{1}{2}k_a(u-g)^2\\
& + A_\infty\left[\alpha - \frac{3}{a} + \frac{3(1-w)^2 + a\,\alpha(1-w)}{a}e^{-\frac{a}{1-w}\alpha}\right].
\end{aligned} \tag{3}$$

Note that the linear elastic phase is characterized by the stiffness coefficient k_a, representing the perfect adherence of the interface, and by the stress threshold τ_0. The nonlinear post-elastic phase has an exponential law with a rate a and an upper bound A_∞. The evolution of wear is governed by the parameters Γ and γ, while $\mathrm{s_w}$ is a boolean function which determines whether the state evolves according to an elastic regime or inelastic, *i.e.*, $\{\dot{g},\ \dot{\alpha},\ \dot{w}\} \neq 0$ only when $\mathrm{s_w} = 1$ (true condition, see eqs. (2)). To ensure the admissibility of the stress state, appropriate consistency conditions must be maintained on the slip function, defined as:

$$F(\tilde{\tau}, A) = ||\tilde{\tau}|| - (\tau_0 + A) \quad \text{with} \quad \tilde{\tau} = \frac{\tau}{1-w}\,. \quad (4)$$

The consistency conditions thus read:

- when $F(\tilde{\tau}, A) < 0$, the interface is in adherence condition, therefore $s_w = 0$, which entails that the internal variables g, α, w do not evolve in time, $\dot{\tau}$ is linear, *i.e.*, eq. (1) reads as $\dot{\tau} = k_a(1-w)\dot{u}$;
- when $F(\tilde{\tau}, A) = 0$, but $\dot{F}(\tilde{\tau}, A) < 0$ the stress state is on the boundary of the slip function, whose evolution in time is negative, thus corresponding to an elastic return phase; same as above, $s_w = 0$ and g, α, w do not evolve in time;
- when $F(\tilde{\tau}, A) = 0$ and $\dot{F}(\tilde{\tau}, A) = 0$ the stress state results on the boundary of the slip function, therefore $s_w = 1$ and g, α, w do evolve in time.

Finally, consistently with the 1-dof nature of the model, the resulting force T associated to τ can be represented as τ multiplied by a nominal contact interface area A_c, thus giving rise to the expression $T = \tau\, A_c$.

2.2 Model parameter identification from experiments

A simple linear displacement ramp $u(t) = u_{\max}/t_{\max} t$ ($u_{\max} = 18$ mm and $t_{\max} = 300$ s) simulating a (pseudo-static) monotonically increasing loading is adopted to identify the constitutive parameters of the proposed model. In particular, we reproduce the experimental outcomes reported in [63]. The results are depicted in Fig. 3 in terms of (a) τ vs. u; (a) g vs. t; (a) α vs. t; (a) w vs. t. The measured response (depicted in red) was obtained to investigate the global behavior of the structure up to failure, thereby pushing the structure beyond the elastic limit to observe plasticity and damage. As expected, the force-displacement curve is first linear, followed by a plastic phase until reaching its maximum value. As the prescribed displacement increases, the global force decreases due to the onset of damage. It's noteworthy that the numerical curve (illustrated in blue) aligns perfectly with the experimental curve in red, see Fig. 3(a). This indicates that the adopted constitutive model effectively captures the global behavior of the considered masonry building. The so identified constitutive parameters will be utilized in subsequent analyses to simulate the global static and dynamic behavior of the single-storey masonry building examined in [63]. We report in Table 1 their values, and in the next Section the resulting responses details.

Note that the interface model, giving rise to the 1-dof system, is constitutively defined in the context of a phenomenological problem of a rigid body sliding on an interface substrate [64,65]. As discussed in the Introduction, the behavior of the entire building should be assessed through numerical investigations or experimental campaigns, modeling it as a multi-dofs system. In the following, we assume that the constitutive parameters of the 1-dof system reported in Table 1 are representative of the more complex friction-based behavior of the whole building: this assumption is consistent with the 1-dof approaches commonly adopted in the literature and technical codes [16–20].

3 Numerical scheme for time integrating of the Equations of Motion

We consider the following equation of motion

$$m\,\ddot{u} + A_c\,\tau(u,\ w,\ g,\ \alpha) = f(t) \quad (5)$$

together with initial value conditions for $u(0)$ and $\dot{u}(0)$. The numerical time integration of this problem is handled by an Explicit Runge-Kutta method. As demonstrated in several studies (see, for instance, [66,67]), this method offers superior performance for problems involving complex constitutive laws, and it is generally regarded as well-suited for any rate-type constitutive model, providing a good balance between the need for high accuracy, strong stability properties, and limited computational costs. Thus, by adopting an explicit Runge-Kutta method of order s, the general formula for the $(n+1)$th time solution can be rewritten as (see, *e.g.*, [68]):

$$\boldsymbol{y}_{n+1} = \boldsymbol{y}_n + h \sum_{i=1}^{s} b_i\, \boldsymbol{k}_i\,, \quad (6)$$

being $\boldsymbol{y} = \{u,\ \dot{u}\}^\top$ the solution vector, and h the time step employed to obtain the $(n+1)$th solution at the time $t_{n+1} = t_n + h$, starting from the known nth solution at the time t_n. The slope $\boldsymbol{k}_i$ at the ith stage is obtained

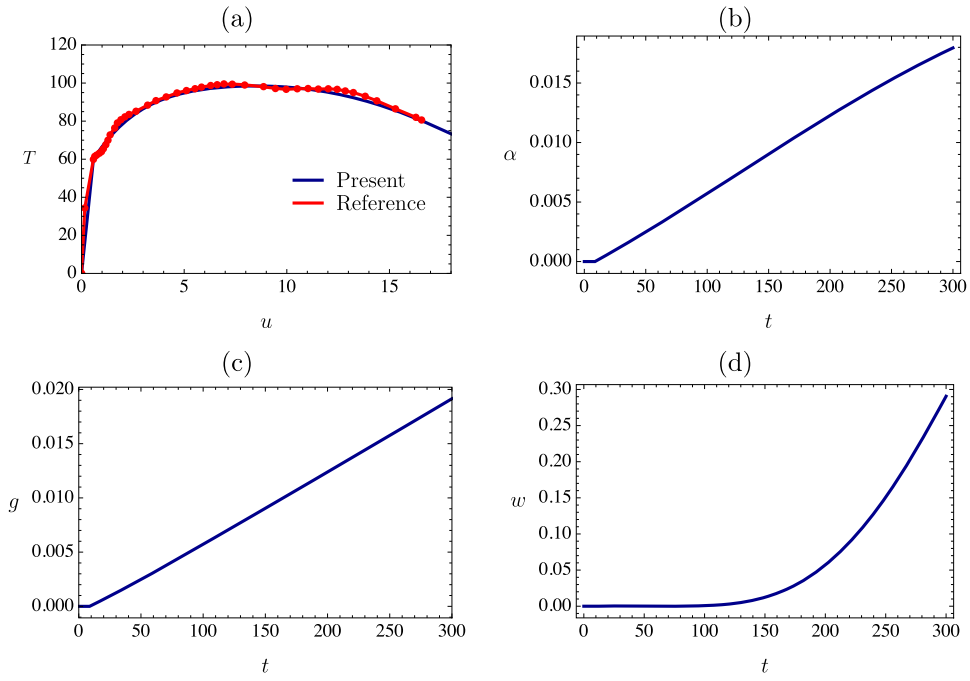

Fig. 3 Identification results (in blue) by comparison with reference experiments in [63] (in red). Force-displacement curves (a), evolution in time of inelastic displacement, hardening and wear variables (b), (c), (d), respectively. Tests obtained by prescribing linear monotonic displacement ramp

Table 1 Interface constitutive parameters

A_c [m^2]	k_a [N/m^3]	τ_0 [N/m^2]	a [1/m]	A_∞ [N/m^2]	Γ [N/m$^{0.5}$]	γ [-]
16.07	6.438×10^6	3734	500	2489	4	2

by the expression

$$\boldsymbol{k}_i = \boldsymbol{f}\left(t_n + c_i\, h,\ \boldsymbol{y}_n + h \sum_{j=1}^{i-1} a_{ij}\, \boldsymbol{k}_j\right), \tag{7}$$

where

$$\boldsymbol{f} = \{\dot{u},\ (f(t) - A_c\, \tau(u,\ w,\ g,\ \alpha))\ /m\}^\top \tag{8}$$

is the vector field of the equation of motion (5) recast into $\dot{\boldsymbol{y}} = \boldsymbol{f}(t,\ \boldsymbol{y})$. The coefficients a_{ij}, c_i and b_i are derived from the so-called *Butcher tableau*, according to the stage s (and then to the order) of the Runge-Kutta method adopted [69]. In particular, the proposed method employs a fourth-order scheme, corresponding to $s = 4$ in eq. (6). The choice of a fourth-order scheme is a widely recognized compromise between accuracy and computational efficiency (see [68]). However, it is well known that these properties are highly sensitive to the time-step size, h, which, in the proposed algorithm, is directly defined by the total number of time steps specified for the analysis. In the next section, we present detailed computations on this aspect, including specific comparisons with other available solvers.

Like most nonlinear material models [59], the constitutive law employed here does not admit an explicit expression of the form $\tau_n = \tau(u_n, w_n, g_n, \alpha_n)$. Instead, the stress τ_n is determined numerically by integrating the rate equations (1) and (2) over time. Following [60–62], we therefore use the approximation induced by the time integration scheme (7). Specifically, we have to compute τ_{k+1} at the time step t_{k+1}, starting from a known value computed at t_k. Assum-

ing a *strain-driven* approach, we initially keep all the internal variables constant at t_k to calculate the stress increment as:

$$\begin{aligned}\tau_{k+1} &= \tau_k + \int_{t_k}^{t_{k+1}} \dot{\tau}(u_k,\, w_k,\, g_k,\, \alpha_k)\,\mathrm{d}t \\ &\approx \tau_k + \Delta\tau(u_k + \Delta u,\, w_k,\, g_k,\, \alpha_k)\,, \end{aligned} \tag{9}$$

and then we evaluate the evolution of the internal variables, thus completing the computation of τ_{k+1} via a procedure of *return mapping*. By doing so, we introduce the quantities governing the internal variable evolutions from (2) respectively as

$$\Delta w = j_{wk}\,\Delta\tau\,, \quad \Delta g = j_{gk}\,\Delta\tau\,, \quad \Delta\alpha = j_{\alpha k}\,\Delta\tau\,, \tag{10a}$$

where

$$\begin{aligned} j_{gk} &:= \partial g_\tau(u_k,\, \Delta u,\, \tau_k + \Delta\tau^{\mathrm{trial}},\, w_k,\, g_k,\, \alpha_k) \\ &= \frac{H_k}{(1-w_k)^2}\,, \\ j_{\alpha k} &:= \partial \alpha_\tau(u_k,\, \Delta u,\, \tau_k + \Delta\tau^{\mathrm{trial}},\, w_k,\, g_k,\, \alpha_k) \\ &= \frac{H_k}{1-w_k}\mathrm{sign}(\tau_k)\,, \\ j_{wk} &:= \partial w_\tau(u_k,\, \Delta u,\, \tau_k + \Delta\tau^{\mathrm{trial}},\, w_k,\, g_k,\, \alpha_k) \\ &= \frac{H_k}{(1-w_k)}\left(\frac{W_k}{\Gamma}\right)^{\gamma}\mathrm{sign}(\tau_k)\,, \end{aligned} \tag{10b}$$

with $\Delta\tau^{\mathrm{trial}}$ being a trial increment of the stress. The correct stress τ_{k+1} is then computed as detailed in Algorithm 1. In particular, the trial stress increment $\Delta\tau^{\mathrm{trial}}$, corresponding to a purely elastic extrapolation associated with the displacement increment Δu, *i.e.*, $\Delta\tau^{\mathrm{trial}} = k_a(1-w_k)\,\Delta u$, is first computed. If the resulting trial stress, $\tau_{k+1} = \tau_k + \Delta\tau^{\mathrm{trial}}$, violates the consistency conditions, *i.e.*, $F_{k+1} \geq 0$ and $\dot{F}_{k+1} \geq 0$, the flow laws (2) and (3) are activated, and the corrected stress increment $\Delta\tau$ can be provided. In fact, the flow laws hold when the inelastic increments can take place , *i.e.*, the consistency conditions are identically satisfied, $F(\tilde{\tau}, A) = 0$ and $\dot{F}(\tilde{\tau}, A) = 0$; the correct stress can be then derived by the equation (1), which can be recast numerically in

$$\Delta\tau = k_a\,(1-w_k)\,(\Delta u - j_{gk}\,\Delta\tau) - k_a\,j_{wk}\,\Delta\tau\,(u_k + \Delta u - g_k)\,, \tag{11}$$

according to (10), and thus solved for $\Delta\tau$.

Algorithm 1 Return-Mapping Algorithm.

function STRESS($u_k,\ \Delta u,\ w_k,\ g_k,\ \alpha_k$)

$\Delta\tau \equiv \Delta\tau^{\mathrm{trial}} = k_a(1-w_k)\,\Delta u$ ▷ purely elastic (trial) step
$\Delta g = \Delta\alpha = \Delta w = 0$
$j_{gk},\ j_{\alpha k},\ j_{wk}$ ▷ assembly rates for internal variables as in (10)
$F_{k+1} := F\left(\frac{\tau_k + \Delta\tau^{\mathrm{trial}}}{1-w_k},\, A_k\right)$, $\dot{F}_{k+1} := \dot{F}\left(\frac{\tau_k + \Delta\tau^{\mathrm{trial}}}{1-w_k},\, A_k\right)$ ▷ compute slip function and its derivative (see eq. (4))

if $F_{k+1} \geq -\mathtt{tol}.$ and $\Delta\tau^{\mathrm{trial}}\dot{F}_{k+1} \geq -\mathtt{tol}.$ **then** ▷ check flow consistency

$\Delta\tau = \dfrac{\Delta\tau^{\mathrm{trial}}}{1 + k_a\,j_{wk}\,(u_k + \Delta u - g_k) + k_a\,j_{gk}\,(1-w_k)}$ ▷ correct stress increment solving (11) for $\Delta\tau$
$\Delta w = j_{wk}\,\Delta\tau$ ▷ correct internal variables
$\Delta g = j_{gk}\,\Delta\tau$
$\Delta\alpha = j_{\alpha k}\,\Delta\tau$

end if

$\tau_{k+1} = \tau_k + \Delta\tau,\ w_{k+1} = w_k + \Delta w,\ g_{k+1} = g_k + \Delta g,\ \alpha_{k+1} = \alpha_k + \Delta\alpha$ ▷ update all variables

return $(\tau_{k+1},\ w_{k+1},\ g_{k+1},\ \alpha_{k+1})$
end function

Note that in Algorithm 1, the numerical tolerance `tol` for accepting violations of the consistency conditions is set to 10^{-6}, which has been found sufficient for the analyses performed. In particular, by applying the same threshold `tol` to both consistency conditions, the second condition $\dot{F}_{k+1} > 0$ is implemented as $\Delta\tau^{\mathrm{trial}}\,\dot{F}_{k+1} \geq -\mathtt{tol}$, thus ensuring that both conditions are numerically consistent.

4 Numerical simulations

All the numerical tests have been conducted on the set of constitutive parameters, reported in Table 1, which we identified as described in Sec. 2.2, according to the behavior experimentally observed by Ravichandran et al. in [63]. Note that, in all the forthcoming figures, time

is expressed in s, the displacement u in m, stresses τ and F in N/m^2, while w is nondimensional.

Initially, numerical simulations are performed in the quasi-static conditions, neglecting inertial forces, in order to validate the algorithm developed to solve the interface equations; both monotonic and cyclic displacement histories are examined. Then, the full dynamic problem is addressed to analyze the system response under both harmonic and random excitations, with seismic actions also taken into account.

It is worth noting that, to enable a clearer comparison between the proposed algorithm and existing solvers, and to emphasize the sensitivity of the overall structural response to accuracy, the proposed algorithm is run with a fixed time-step size h.

4.1 Comparative benchmarking

Preliminary validation

Three sets of numerical tests are carried out to investigate the numerical stability of the proposed strategy by considering different displacement loading histories. The solution is systematically compared with that obtained via well-known and powerful solvers of commercial softwares, *i.e.*, `Wolfram Mathematica` and `MATLAB`. Specifically, in the former we employ the `NDSolve` numerical solver in conjunction with the `WhenEvent` function for handling the changes in the behavior of the ODE system for satisfying the consistency conditions discussed in Sec. 2.1; analogously, in the latter the `ode45` solver is combined with the `Events` option function.

The considered sets of loading conditions are reported in Table 2. In particular, three sets of numerical tests were conducted to investigate the numerical stability of the proposed strategy across different displacement loading histories. The tests cover a range of loading conditions, all conducted over a time interval $[0, t_{\max}]$, with $t_{\max} = 500$ s.

The analysis reveals that for the monotonic and cyclic ramps 1 and 2 of Set 1, represented by purely linear and purely sinusoidal functions over time, respectively, the results of the proposed numerical scheme align perfectly with those from `NDSolve` and `ode45` solvers, as shown in the pairs of plots (a), (b) and (c), (d) in Fig. 4.

However, a noticeable deviation occurs with ramp 3, which involves approximately doubling the sinusoidal load frequency, as illustrated in subplots (e) and (f) of Fig. 4. This discrepancy is attributed to an accelerated damage velocity induced by the higher load frequency. Notably, both standard solvers exhibit signs of numerical instability, indicated by warning messages alerting to typical issues such as low numerical stability and ill-conditioned matrices involved in the computations.

In this context, the proposed code reveals to be a reference solution as proved by a convergence analysis conducted on the Test Set 1 ramp 3 by varying the number of steps in the range $n_{step} = [400,\ 20000]$, see Fig. 5. The figure illustrates the percentage variation of the final damage value, Δw, evaluated with respect to the number of time steps. For $n_{\text{step}} > 2000$, the variation in w remains below 1%. As a side note, this result demonstrates the robustness of the algorithm concerning the choice of step size.

Focused Benchmarking

To better understand the numerical stability issues of the `Matlab` solver, additional comparisons are performed using various alternative solvers. The analyses focus on Test Set 1, ramp 3, with the results summarized in Table 3, which reports the number of time steps required to reach $t_{\max}$ and the percentage variation Δw in the final damage value. Specifically, Δw represents the difference between the final value of w computed by the ith solver and the reference value obtained with the algorithm proposed in this work. It is important to note that all values of Δw reported in Table 3 are negative, indicating that the final damage predicted by the `Matlab` solvers is consistently lower than the reference solution.

The results reveal that the solvers `ode23s` and `ode15i` are unable to handle this type of problem. The solver `ode15s` provides a response very similar to that of the previously used `ode45`; however, both fail to accurately detect the transitions between the linear and nonlinear regimes, leading to a significant error in the overall response, *i.e.*, more than 45%. On the other hand, the solvers `ode23`, `ode113`, `ode78`, and `ode89` are able to accurately capture the transitions between the adherence and slip phases, providing results in good agreement with those obtained from the in-house code, with an error of less than 1%.

However, the accuracy of the various solvers cannot be assessed solely by monitoring the final value of w. As it will be described in more details next, the switch between the adherence phase and the slip phase is identified when the slip function approaches zero. This

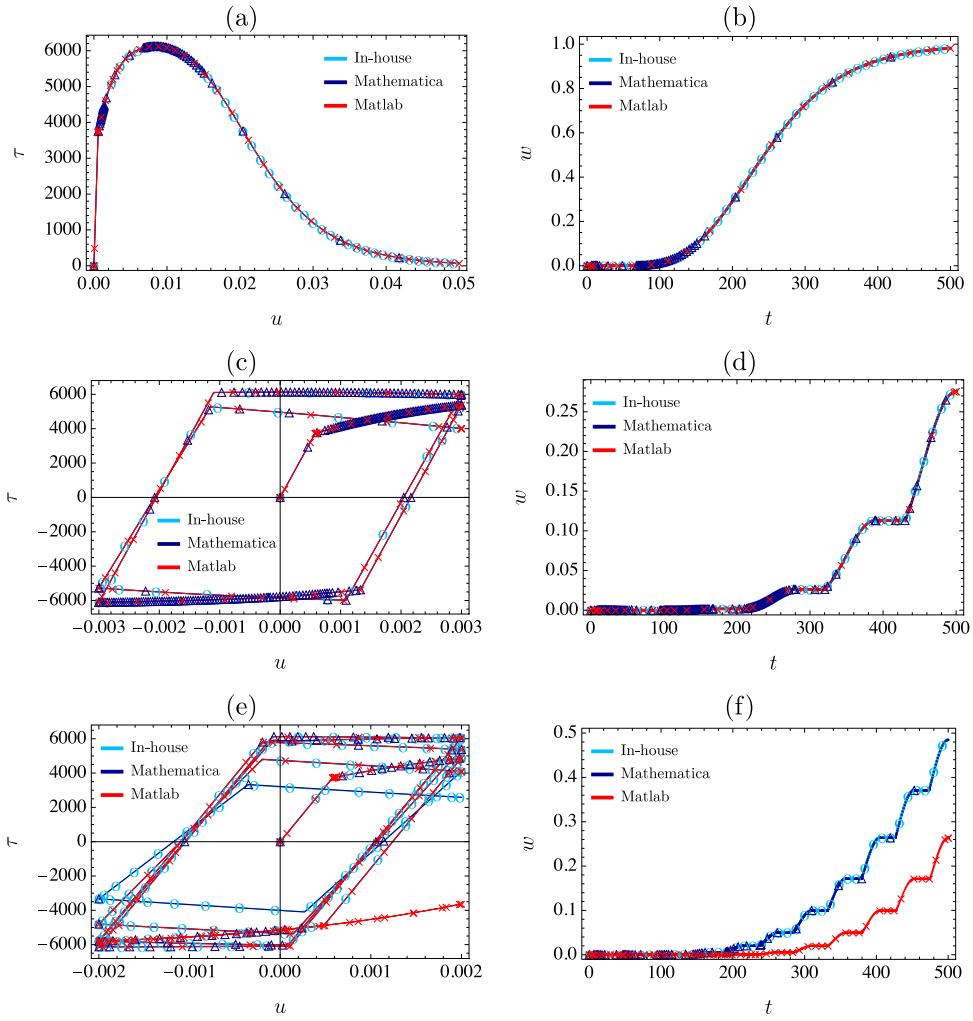

Fig. 4 Test Set 1, see Table 2: (a),(b) ramp 1; (c), (d) ramp 2; (e), (f) ramp 3. In the left column, stress-displacement curves (τ, u); in the right column, wear damage evolution in time (w, t). Results obtained by the proposed solver (cyan) compared with `Wolfram Mathematica` and `MATLAB` (dark and light blue, respectively)

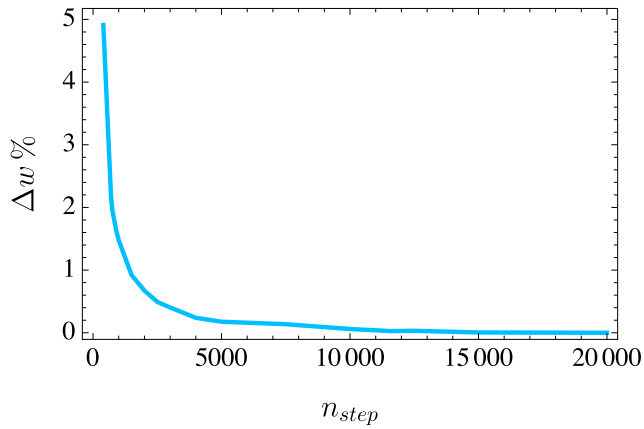

Fig. 5 Convergence analysis of the in-house code with reference to the number of steps n_{step}

Table 2 Description of test sets and associated loading ramps, all working with a time integration over the time interval $[0,\ t_{\max}]$ with $t_{\max} = 500$ s. Displacement values $u_{\max}$ in mm

Test Set	loading expression		main pars.
Test Set 1: preliminary monotonic and cyclic ramps			
	ramp 1:	$u(t) = \frac{u_{\max}}{t_{\max}}\, t$	$u_{\max} = 50$
	ramp 2:	$u(t) = u_{\max}\ \sin(\omega_f t)$	$\omega_f = \frac{\pi/2+2\pi k}{t_{\max}}$, $k = 2$, $u_{\max} = 3$
	ramp 3:	$u(t) = u_{\max}\ \sin(\omega_f t)$	$\omega_f = \frac{\pi/2+2\pi k}{t_{\max}}$, $k = 5$, $u_{\max} = 2$
Test Set 2a: cyclic ramps with linearly increasing amplitude up to $u_{\max} = 1$			
	ramp 1:	$u(t) = \frac{u_{\max}}{t_{\max}}\, t\ \sin(\omega_f t)$	$\omega_f = \frac{\pi/2+2\pi k}{t_{\max}}$, $k = 1$
	ramp 2:	$u(t) = \frac{u_{\max}}{t_{\max}}\, t\ \sin(\omega_f t)$	$\omega_f = \frac{\pi/2+2\pi k}{t_{\max}}$, $k = 3$
	ramp 3:	$u(t) = \frac{u_{\max}}{t_{\max}}\, t\ \sin(\omega_f t)$	$\omega_f = \frac{\pi/2+2\pi k}{t_{\max}}$, $k = 4$
Test Set 2b: cyclic ramps with nonlinearly increasing amplitude up to $u_{\max} = 1$			
	ramp 1:	$u(t) = u_{\max} \left(\frac{t}{t_{\max}}\right)^{\beta} \sin(\omega_f t)$	$\omega_f = \frac{\pi/2+2\pi k}{t_{\max}}$, $k = 3$, $\beta = 1.25$
	ramp 2:	$u(t) = u_{\max} \left(\frac{t}{t_{\max}}\right)^{\beta} \sin(\omega_f t)$	$\omega_f = \frac{\pi/2+2\pi k}{t_{\max}}$, $k = 3$, $\beta = 0.75$
Test Set 3: convergence analysis to time step (only in-house code considered)			
	same as ramp 2, Set 2b		

Table 3 Comparison between the different ode solvers in terms of the number of time steps n_{step} and the percentage difference $\Delta w\%$ in the final value of the damage variable w, relative to the reference solution obtained with the proposed algorithm

Solver	n_{step}	$\Delta w\%$
`Mathematica`	5587.	0.1087
`Matlab ode45`	1449.	45.6362
`Matlab ode23`	7942.	0.0992
`Matlab ode113`	1038.	0.0992
`Matlab ode78`	921.	0.0992
`Matlab ode89`	985.	0.0992
`Matlab ode15s`	1813.	45.6362
`Matlab ode23s`	na	na
`Matlab ode23t`	14782.	0.0992
`Matlab ode23tb`	11142.	0.0992
`Matlab ode15i`	na	na

marks a critical point, which can introduce errors whenever the solver must handle this event, *i.e.*, determining the exact moment at which the state change occurs. To better highlight this type of difficulties encountered by these solvers, the time history of F is shown in Fig. 6(a). It can be noted that the in-house code and the `NDSolve` are in good agreement, whereas the solution given by `ode45` remains in the nonlinear phase, thus missing two elastic return phases. Fig. 6(b) instead shows the difference between F evaluated in the `ode45` (red), `ode23` (green), `ode15s` (magenta), and that obtained via the in-house code, reported as a fraction of τ_0. As discussed above, solvers `ode45` and `ode15s` fully overlap and are affected by errors above 30%, while, despite giving an overall good response, solver `ode23` is also characterized by an error of approximately 5%. The error given by the remaining solvers `ode113`, `ode78` and `ode89` is not reported here, since it is very similar (overlapping) to that given by `ode23`.

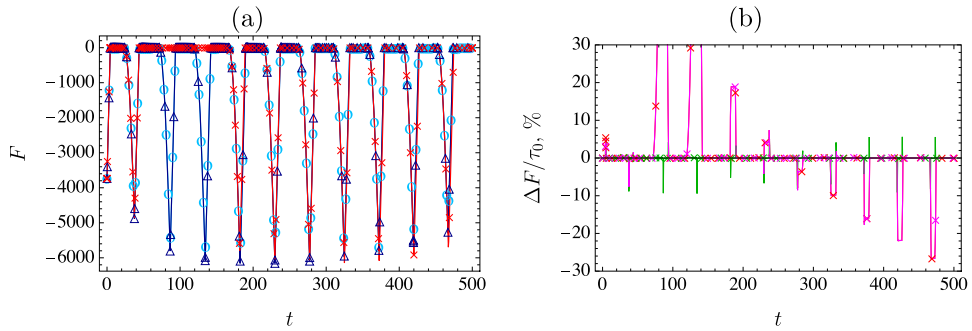

Fig. 6 On the left (a): time history of F for Test Set 1 ramp 3 (see Table 2) using the same three solvers shown in Fig. 4. On the right (b): time history of the percentage difference between F computed by the ith solver (`ode45` in red, `ode23` in green, `ode15s` in magenta) and the in-house code, expressed as a fraction of τ_0

As a final remark, it should be clarified that all `Matlab` solvers require the use of the `Events` subroutine to identify the time instants at which a transition between the elastic and slip phases occurs. When the subroutine successfully detects these events and evaluates the solution at the corresponding time, it halts the integration process. Consequently, to compute the entire time history, each `Matlab` solver must be embedded within an external loop that manually restarts the integration from updated initial conditions after each event. This, combined with the need for ad hoc solver parameter tuning, makes the `Matlab`-based approach significantly more problem-dependent compared to the method proposed in this work.

Stability and Convergence Analysis

To address the issues of numerical instability encountered with standard solvers like `NDSolve` and `ode45`, especially under conditions like ramp 3, there are recognized strategies. These involve adjustments to solver parameter settings or appropriate rescaling of the problem's equations. However, such solutions might not align well with the aims of this study, which seeks to propose an efficient solution method that is straightforward to implement in a low-level programming language and suitable for specific hardware environments. Given this context, we decide to focus on using `NDSolve` exclusively as a benchmark. This decision is guided by the intention to simplify comparisons and underscore the practical advantages of the proposed approach in terms of stability and accuracy.

In Fig. 7, utilizing the functions defined by Set 2a, we delve into the impact of damage velocity on the stress response by examining a sinusoidal loading history with a linearly increasing amplitude and loading frequency. The analysis focuses on two energy variables, $E_{\text{int}} = \int_0^{t_{\max}} A\tau\,\dot{u}\,\mathrm{d}t$ and W, which represent the internal work performed by the stress τ and the wear energy associated with the damage variable w, respectively. As energy quantities, their evolution over time offers valuable insights, albeit indirectly, into the numerical stability of the solvers.

For comparison purposes, the proposed solver is set to execute the same number of steps as `NDSolve`, which employs adaptive step-size procedures, whereas the proposed method uses a constant step-size.

Plots (a)–(d) in Fig. 7 illustrate that at a moderate loading frequency, the energy responses from both solvers align perfectly, affirming stable behavior. However, as the loading frequency increases by approximately 30%(from $k = 3$ to $k = 4$), the response from `NDSolve` starts to diverge, while the proposed code maintains a coherent behavior comparable to that at lower loading frequencies, as depicted in Fig. 7(e) and Fig. 7(f).

Similar performance are achieved when the damage velocity is modulated by keeping the loading frequency constant and by growing nonlinearly the amplitude of the sinusoidal loading condition, ranging from slower to faster than linear growth. This approach allows for the examination of the solver adaptability to changes in the rate of damage accumulation without altering the cyclic frequency of the applied load.

This dynamic is illustrated in Fig. 8, based on the functions outlined in Set 2b. For scenarios where the loading amplitude increases with an exponent of 1.25, both `NDSolve` and the proposed solver exhibit compa-

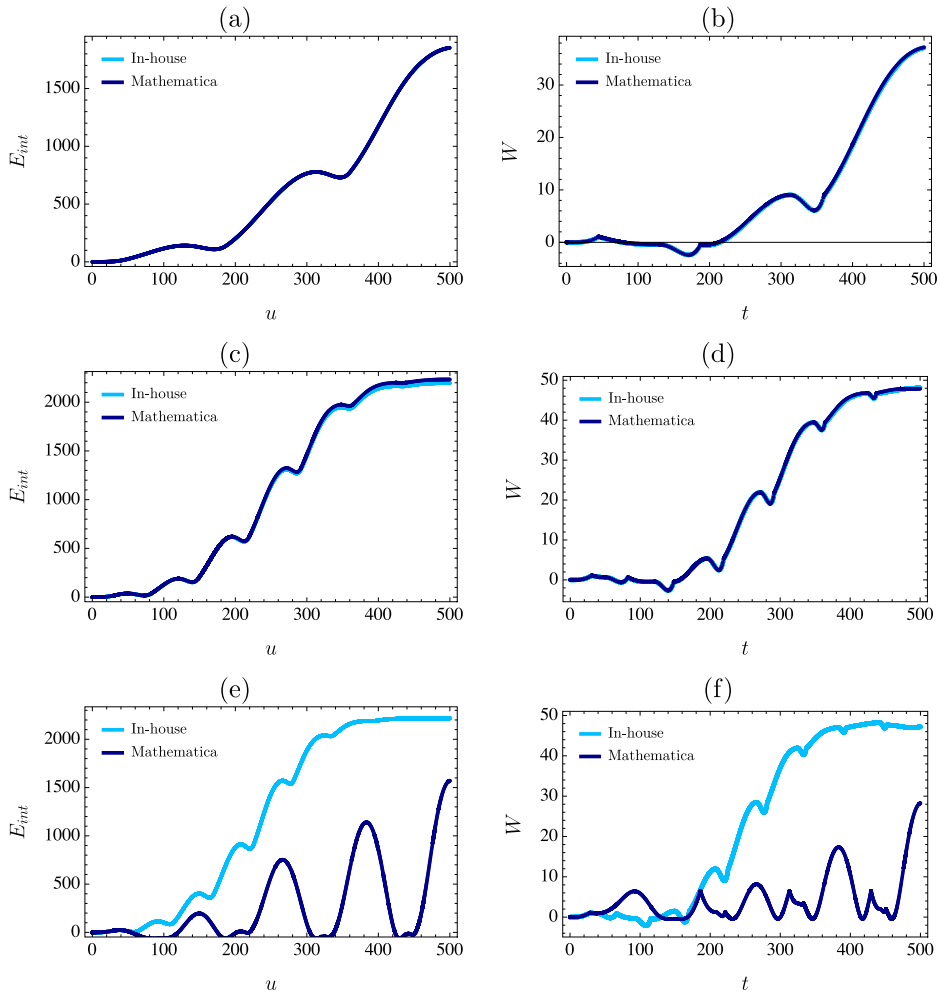

Fig. 7 Test Set 2a, see Table 2: (a),(b) ramp 1; (c), (d) ramp 2; (e), (f) ramp 3. In the left column, evolution in time of the internal work E_{int}; in the right column, evolution in time of the damage-associated energy W. Results obtained by the proposed solver (cyan) compared with `Wolfram Mathematica` (dark blue)

rable performances, as shown in plots (a) and (b). This indicates a stable and consistent energy response from both solvers under conditions of moderately accelerated loading amplitudes.

However, a different picture emerges when the amplitude growth exponent is reduced to 0.75, representing a more gradual increase in loading amplitude. In this scenario, `NDSolve` exhibits a divergent energy response, suggesting potential instability or an inability to accurately capture the effects of sub-linear growth in loading amplitude. In contrast, the proposed solver maintains the expected behavior, delivering a coherent and stable response to the varying loading conditions, as shown in curves (c) and (d) of Fig. 8.

To delve into the stability and convergence performance of the proposed numerical scheme, we explore the last type of loading histories (Set 2b, ramp 2) by employing different values of time step sizes. Specifically, we use $\{1/2,\ 2,\ 4\}\,\overline{\Delta t}$, where $\overline{\Delta t}$ denotes the average time step size calculated to ensure an equal number of time steps as those provided by `NDSolve`. The outcomes of this investigation are illustrated in Fig. 9.

The in-house code proves to be able to effectively reproduce the same curves even with the coarsest

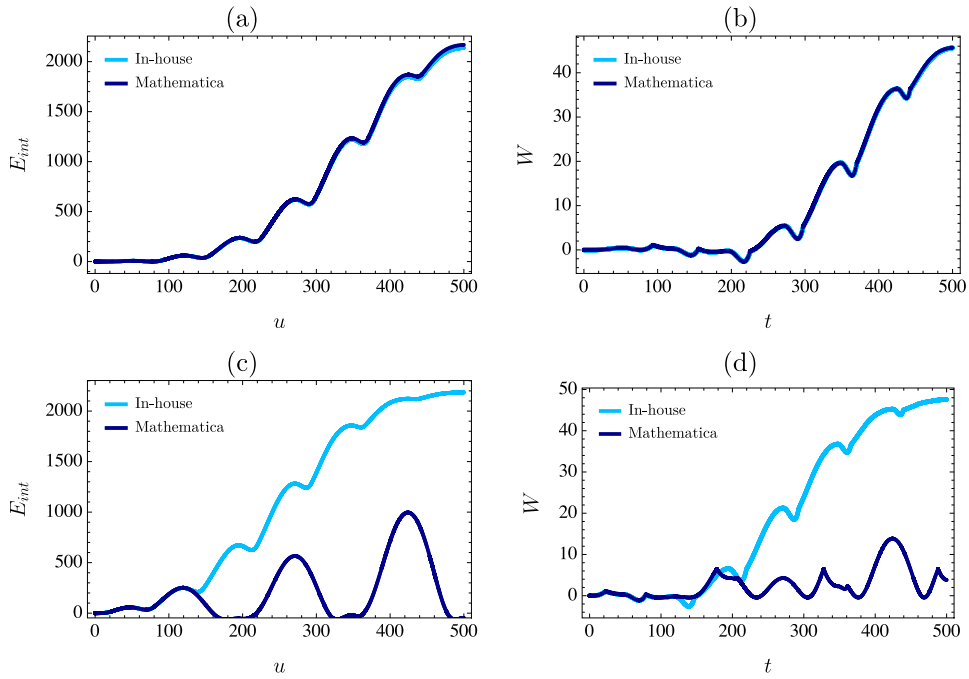

Fig. 8 Test Set 2b, see Table 2: (a),(b) ramp 1; (c), (d) ramp 2. In the left column, evolution in time of the internal work E_{int}; in the right column, evolution in time of the damage-associated energy W. Results obtained by the proposed solver (cyan) compared with `Wolfram Mathematica` (dark blue)

time discretization, unless some slight variations in the energy plots of Fig. 9(a) and Fig. 9(b). These differences mainly appear near the switching points of loading/unloading paths, as evident in the zoomed stress-vs-time curves featured in plots (c) and (d) of Fig. 9. Remarkably, even with a time discretization that is four times coarser, these plots unveil only a negligible 3% discrepancy in the stress response.

This analysis highlights the robustness of the proposed numerical scheme, demonstrating its ability to maintain accuracy and stability across a range of discretization levels. The minor deviations observed at critical transition points in the loading history underscore the importance of time step selection in capturing the intricate dynamics of the system, while also affirming the method's overall reliability and effectiveness in simulating complex loading conditions.

4.2 Application-oriented tests

This section investigates the system response under real seismic actions, with particular attention to the effects of accumulated damage due to multiple successive events. To this end, the full dynamic problem is addressed by the proposed numerical strategy, thus analyzing the behavior under different loading conditions: both single and multi-frequency harmonic excitations, random excitations, and eventually seismic excitation sequences.

Harmonic excitations

The dynamic response of the system is initially investigated under a single harmonic excitation, *i.e.*, $f(t) = A_f \cos \Omega_f t$. Posing that the natural frequency of the 1-dof oscillator is defined as $\omega_0 = \sqrt{A_c\, k/m}$, the dynamic force is adjusted to induce resonance by setting $\Omega_f = \omega_0$.

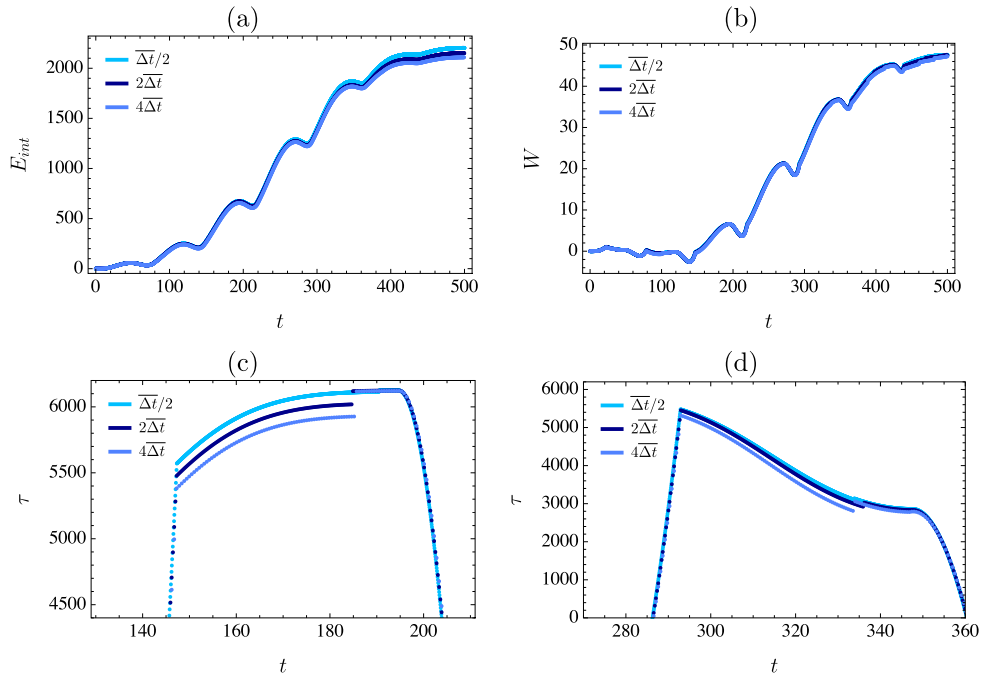

Fig. 9 Test Set 3, see Table 2: (a),(b) ramp 1; (c), (d) ramp 2. In the first row, evolution in time of energy variables, namely E_{int} (a) and W (b); in the second row, subset of the evolution in time of τ. Solutions obtained with the proposed solver by considering different time step sizes

As previously noted in [70], the onset of damage leads to a reduction in the oscillator frequency, as reflected by the increase in the damage variable w, causing a detuning from the excitation frequency. This phenomenon results in the system behaving similarly to a damped oscillator, which eventually reaches a steady-state response characterized by an hysteretic force-displacement diagram. In this state, damage progression halts. Essentially, the system's plasticity and damage mechanisms serve to dissipate energy, allowing for the stabilization of the system response despite the initial resonance conditions.

In Fig. 10(a), the time evolution of the damage variable w is depicted, revealing that it stabilizes to a constant value after a certain period. This indicates that the oscillator has entered a damped harmonic response phase (not shown here), prompting further investigation under excitations with multiple frequencies near the oscillator natural frequency. To explore this, an excitation of the form $f(t) = \frac{A_f}{3}\left(\cos\Omega_f t + \cos 0.95\Omega_f t + \cos 0.9\Omega_f t\right)$ is also considered. This configuration allows for resonance maintenance and delays detuning as damage progresses and the oscillator's frequency decreases. The smallest frequency components of $f(t)$ remain in resonance with the system even as its natural frequency shifts due to damage accumulation.

As illustrated in Fig. 10(b), the system continues to accumulate damage. This indicates that excitations with multiple frequencies can lead to significant damage evolution even if the average amplitude of the excitation is not necessarily high. The presence of multiple frequencies enables continuous resonance with the evolving system, thereby increasing the damage under conditions that might not be as damaging with a single-frequency excitation.

Random excitations

Building on the insights gained from the previous section, the focus now shifts to understanding system behavior under random excitations, such as seismic actions. To explore this, the system response to a random base excitation is examined. Specifically, the force applied to the system is modeled as $f(t) = -ma_g(t)$, where $a_g(t)$ represents the ground acceleration. The system response is depicted in Fig. 11 in terms of (a), (b)

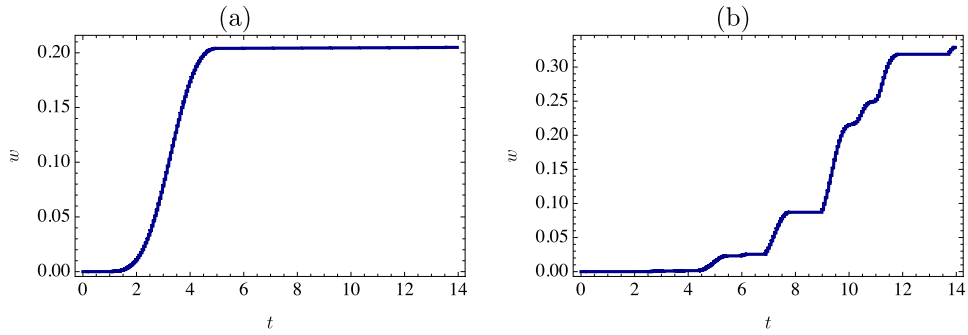

Fig. 10 Damage time evolution under harmonic load with same overall excitation amplitude and different frequency spectrum, (a) $f(t) = A_f \cos \Omega_f t$, (b) $f(t) = \frac{A_f}{3}\left(\cos \Omega_f t + \cos 0.95\Omega_f t + \cos 0.9\Omega_f t\right)$, respectively

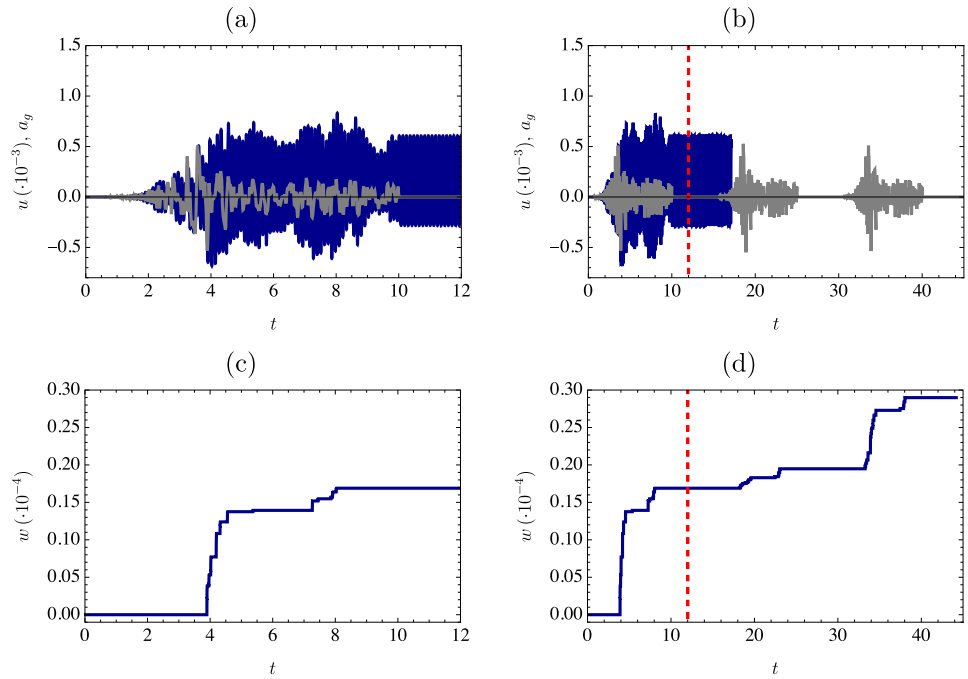

Fig. 11 System response under random base excitation, curves in blue line: (a), (b) displacement vs. time, and (c), (d) damage vs. time. Gray lines in (a), (b) denote the selected ground acceleration; in (b), (d) the dashed red gridline indicates the time at which the first signal ends

displacement (blue line) and (c), (d) damage. Specifically, a single seismic event is considered in graphs (a) and (c) of Fig. 11, where both displacement and damage evolve over time until the signal ceases, resulting in the oscillator undergoing linear undamped free oscillations while damage levels off.

Conversely, when the system is subjected to three independent subsequent accelerograms (the same signal repeated), it's observed that the second and third occurrences lead to larger oscillations and further damage, as shown in graphs (b) and (d) of Fig. 11. In this scenario, a noticeable increase in damage is observed, despite the three subsequent events comprising the same acceleration signal. This highlights the cumulative effect of repeated seismic events on the structural integrity of the system, emphasizing the importance of considering such scenarios in seismic resilience and damage assessment studies.

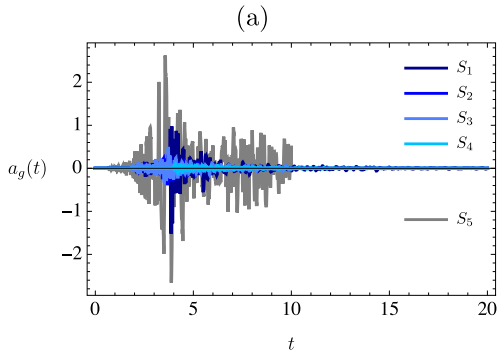

(b)

	PGA m/s^2	RMS m/s^2	AI $m/s\ (\cdot 10^2)$
S_1	1.56	0.097	4.35
S_2	0.39	0.030	0.44
S_3	0.50	0.036	0.60
S_4	0.12	0.013	0.08
S_5	2.75	0.315	48.10

Fig. 12 Accelerograms from the seismic sequence of the L'Aquila earthquake (a), corresponding to the four most significant foreshocks $\{S_1, \ldots, S_4\}$ after followed by the primary shock S_5 [71]. Seismic intensity measures (b) associated with the considered foreshocks [72] , with AI representing the Arias Intensity

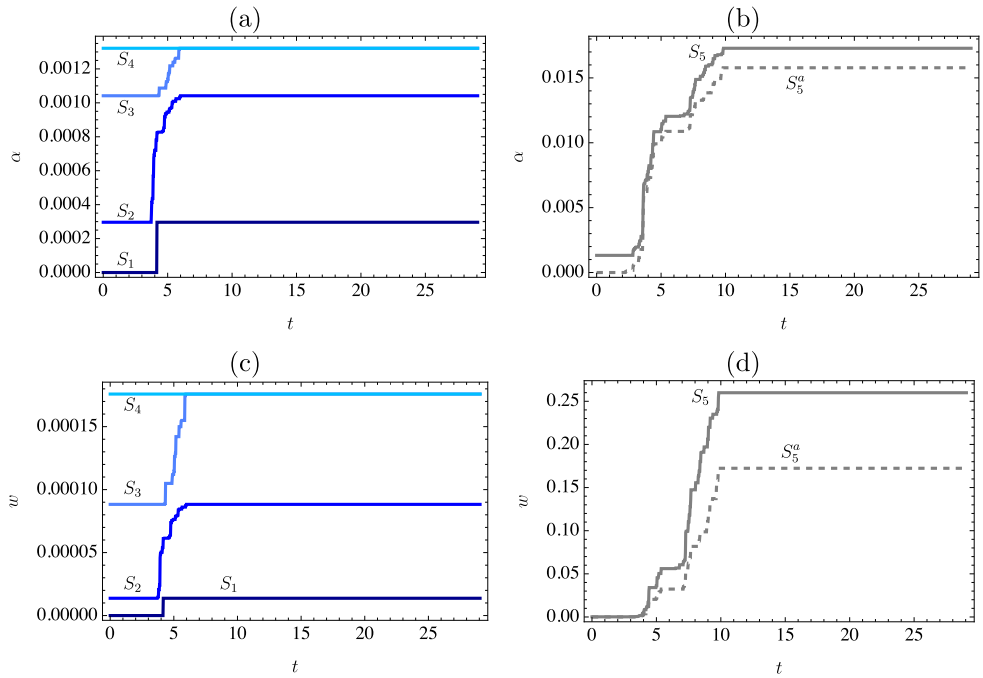

Fig. 13 System response to the seismic accelerograms in Fig. 12. Left column: the accumulated α (a) and w (c) in time during the foreshocks $S_{1,4}$. Right column: the accumulated α (b) and w (d) in time as a consequence of the primary shock considered as a single event S_5^a (dashed gray line) and as a consequence of the full seismic sequence S_5 (solid gray line)

It should be noted from Fig. 11 that, after the input signal stops, undamped free vibrations are observed. This occurs because the oscillator is vibrating in its linear regime, as dissipation is not considered in the model. Indeed, the focus here is specifically on analyzing the behavior of the oscillator by considering the nonlinear constitutive response as the sole source of dissipation. Naturally, other phenomena (*e.g.*, soil-structure interaction, clearance/impact in connections, and so on), which are not considered in the present study, could introduce additional dissipation, potentially modeled as linear viscous damping.

Seismic sequence

The analyses conducted thus far lay the groundwork for simulating seismic sequences that are typical of real events, where minor shocks often precede or follow a major earthquake. Such sequences are characterized by multiple low-amplitude events that, when considered individually, may not appear to pose significant threats to structural integrity. In contrast, the proposed model captures a damage accumulation process that can progressively evolve, even under minor, repeated, seismic events. This can lead to compounded structural effects and, in some cases, premature failures that might not have been anticipated if only the isolated impacts of minor events or the main shock were considered.

For the subsequent analyses, the seismic sequence leading up to the L'Aquila earthquake, documented in [71], serves as the test case. The sequence involves strikes 1-4 (foreshocks) followed by the primary shock. The input signals, *i.e.*, the ground accelerations, are illustrated in Fig. 12(a), with the key characteristics of the signals summarized in Fig. 12(b), where AI index represents the Arias Intensity, see [72].

The dynamic nonlinear response of the system is showcased in Fig. 13 through the variables α and w. Specifically, the left column depicts the response up to the fourth shock (S_1 to S_4), whereas the right column shows the response to the main shock S_5 following the sequence (solid gray line). This response is compared to a hypothetical scenario where S_5 acts alone (dashed gray line), assuming no prior plasticity or damage.

Notably, the seismic sequence induces minor plasticity and damage to the structure. As a result, by the time the main shock occurs, the system already possesses non-zero initial values of α and w, leading both plasticity and damage to gradually accumulate over time. Specifically, α sees a 9% increase, while the damage variable w ends up 50% greater than it would have been had the main shock occurred individually. This highlights the significant impact of seismic sequences on the structural integrity and the critical importance of accounting for such sequences in seismic analysis and design.

5 Conclusions

This study introduces a numerical strategy for both fast and robust simulations of the nonlinear dynamic behavior of masonry buildings subjected to general external time-dependent loads. To optimize solvers for fast computations suitable for seismic structural health monitoring in large-scale urban contexts, a 1-dof model incorporating a nonlinear constitutive law that accounts for plasticity and damage induced by friction and wear is employed. The solution is obtained numerically through a custom-developed algorithm designed to handle the piece-wise nonlinear equations effectively. The code, implemented in `C++`, is capable of running on common hardware and microcontrollers (*e.g.*, Arduino, Asus Tinker Board, Raspberry Pi), and is publicly available at https://zenodo.org/records/10808423.

The model was validated in pseudo-static regimes based on the experimental behavior of a real-scale single-storey masonry building. Subsequently, the numerical stability of the developed algorithm was assessed under both static and dynamic conditions by comparison with standard numerical solvers found in popular commercial software like `Wolfram Mathematica` and `MATLAB`. Despite employing a fixed time-step size, the proposed solver demonstrated high stability across a variety of loading conditions, outperforming standard solvers in different scenarios. Moreover, it accurately converged to the expected solution, even as the time discretization was progressively coarsened.

The investigation further explored the response to seismic sequences that typically affect real buildings, highlighting the accumulation of damage and plasticity after each seismic event. Notably, the outcome after a sequence of seismic events differs significantly from that of a solitary strong shock. The pre-existing damage and plasticity alter the initial conditions when the main shock occurs, leading to significantly increased damage.

In future work, the authors plan to apply the proposed strategy to monitor real cases, including the seismic impact at the urban scale of ancient towns in Italy. Given the demonstrated vulnerability of historic centers and their lack of seismic resilience, this research addresses an urgent need for advanced and efficient methods. These methods aim to provide municipalities with effective tools for seismic vulnerability assessment, especially pertinent in Italy, where recent seismic activities have underscored the critical challenge of enhancing structural resilience.

Author contributions All authors equally contributed to the preparation of the manuscript.

Funding Open access funding provided by Università degli Studi Roma Tre within the CRUI-CARE Agreement. This work was partially funded by the research project PRIN PNRR 2022 grant n. P2022339JP (CUP F53D23009550001).

Data Availability Statement No datasets were generated or analysed during the current study.

Declarations

Conflicts of Interest The authors declare no conflict of interest.

References

1. Hernandez, E.M., Erazo, K.: Lower bound of structural damage to achieve practical identifiability of nonlinear models in seismic structural health monitoring. Earthquake Engineering & Structural Dynamics **53**(1), 5–22 (2024). https://doi.org/10.1002/eqe.4011
2. Kouris, L.A.S., Penna, A., Magenes, G.: Seismic damage diagnosis of a masonry building using short-term damping measurements. Journal of Sound and Vibration **394**, 366–391 (2017)
3. Dragos, K., Magalhães, F., Manolis, G.D., Smarsly, K.: Frequency-domain synchronization of structural health monitoring data. Journal of Sound and Vibration **571**, 118017 (2024)
4. Nayyerloo, M., Chase, J., MacRae, G., Chen, X.-Q.: Lms-based approach to structural health monitoring of nonlinear hysteretic structures. Structural Health Monitoring **10**(4), 429–444 (2010). https://doi.org/10.1177/1475921710379519
5. Formisano, A., Florio, G., Landolfo, R., Mazzolani, F.M.: Numerical calibration of an easy method for seismic behaviour assessment on large scale of masonry building aggregates. Advances in Engineering Software **80**, 116–138 (2015). https://doi.org/10.1016/j.advengsoft.2014.09.013
6. Brando, G., De Matteis, G., Spacone, E.: Predictive model for the seismic vulnerability assessment of small historic centres: Application to the inner abruzzi region in italy. Engineering Structures **153**, 81–96 (2017). https://doi.org/10.1016/j.engstruct.2017.10.013
7. Chieffo, N., Formisano, A.: Induced Seismic-Site Effects on the Vulnerability Assessment of a Historical Centre in the Molise Region of Italy: Analysis Method and Real Behaviour Calibration Based on 2002 Earthquake. Geosciences **10**(1), 21 (2020). https://doi.org/10.3390/geosciences10010021
8. Garavaglia, E., Angjeliu, G., Cardani, G.: Simplified seismic vulnerability analysis of historic residential buildings with fragility curves. Procedia Structural Integrity **44**, 155–162 (2023) https://doi.org/10.1016/j.prostr.2023.01.021. XIX ANIDIS Conference, Seismic Engineering in Italy
9. Acito, M., Buzzetti, M., Cundari, G.A., Milani, G.: General methodological approach for the seismic assessment of masonry aggregates. Structures **57**, 105177 (2023). https://doi.org/10.1016/j.istruc.2023.105177
10. Wang, P., Milani, G.: Seismic vulnerability prediction of masonry aggregates: Iterative finite element upper bound limit analysis approximating no tensile resistance. Engineering Structures **293**, 116595 (2023). https://doi.org/10.1016/j.engstruct.2023.116595
11. Ruggieri, S., Liguori, F.S., Leggieri, V., Bilotta, A., Madeo, A., Casolo, S., Uva, G.: An archetype-based automated procedure to derive global-local seismic fragility of masonry building aggregates: Meta-forma-xl. International Journal of Disaster Risk Reduction **95**, 103903 (2023). https://doi.org/10.1016/j.ijdrr.2023.103903
12. Vailati, M., Monti, G.: Low-lod fragility curves of structural units in masonry building clusters for territorial risk analysis. Engineering Structures **286**, 116143 (2023). https://doi.org/10.1016/j.engstruct.2023.116143
13. Cinque, D., Spina, D., Capua, R., Antonetti, D., Gabriele, S.: Application of innovative high accuracy gnss based system to the monitoring of civil structures. In: European Workshop on Structural Health Monitoring, pp. 61–70 (2022). Springer
14. Xu, Z., Zhu, Y., Gu, D., Zhou, Q.: An integrated simulation method for large-scale earthquake-induced falling debris in building groups. Earthquake Engineering & Structural Dynamics, 1–20 (2024) https://doi.org/10.1002/eqe.4090
15. Sivaselvan, M.: Hysteretic models with stiffness and strength degradation in a mathematical programming format. International Journal of Non-Linear Mechanics **51**, 10–27 (2013)
16. Zou, X., Gong, M., Zuo, Z., Liu, Q.: An efficient framework for structural seismic collapse capacity assessment based on an equivalent sdof system. Engineering Structures **300**, 117213 (2024). https://doi.org/10.1016/j.engstruct.2023.117213
17. Magliulo, G., D'Angela, D.: Seismic response and capacity of inelastic acceleration-sensitive nonstructural elements subjected to building floor motions. Earthquake Engineering & Structural Dynamics **53**(4), 1421–1445 (2024). https://doi.org/10.1002/eqe.4080
18. Applied Technology Council: Seismic Evaluation and Retrofit of Concrete Buildings, Report No. SSC 96-01: ATC-40. (1996). Applied Technology Council
19. Building Seismic Safety Council: NEHRP Commentary on the Guidelines for the Seismic Rehabilitation of Buildings, FEMA Publication 274, ATC-33 Project. (1997). Building Seismic Safety Council
20. Public Works (M.D.), I.M.D.: New Technical Codes for Constructions (in Italian). Official Gazette of the Italian Republic n. 42 published on 2018, February 20th, (2018).

Official Gazette of the Italian Republic n. 42 published on 2018, February 20th
21. Mazzon, N., Chavez, C.M., Valluzzi, M.R., Casarin, F., Modena, C.: Shaking table tests on multi-leaf stone masonry structures: Analysis of stiffness decay. Advanced Materials Research **133-134**, 647–652 (2010) https://doi.org/10.4028/www.scientific.net/amr.133-134.647
22. Magenes, G., Penna, A., Senaldi, I.E., Rota, M., Galasco, A.: Shaking table test of a strengthened full-scale stone masonry building with flexible diaphragms. International Journal of Architectural Heritage **8**(3), 349–375 (2013). https://doi.org/10.1080/15583058.2013.826299
23. Vintzileou, E., Mouzakis, C., Adami, C.-E., Karapitta, L.: Seismic behavior of three-leaf stone masonry buildings before and after interventions: Shaking table tests on a two-storey masonry model. Bulletin of Earthquake Engineering **13**(10), 3107–3133 (2015). https://doi.org/10.1007/s10518-015-9746-x
24. Giaretton, M., Ingham, J.M., Dizhur, D.: Shaking table testing of two storey as-built and retrofitted scaled urm buildings. Structures **41**, 260–269 (2022). https://doi.org/10.1016/j.istruc.2022.04.098
25. Tomić, I., Penna, A., DeJong, M., Butenweg, C., Correia, A.A., Candeias, P.X., Senaldi, I., Guerrini, G., Malomo, D., Beyer, K.: Shake table testing of a half-scale stone masonry building aggregate. Bulletin of Earthquake Engineering (2023). https://doi.org/10.1007/s10518-023-01810-y
26. Brasile, S., Casciaro, R., Formica, G.: Multilevel approach for brick masonry walls - part i: A numerical strategy for the nonlinear analysis. Computer Methods in Applied Mechanics and Engineering **196**(49), 4934–4951 (2007). https://doi.org/10.1016/j.cma.2007.06.021
27. Brasile, S., Casciaro, R., Formica, G.: Finite element formulation for nonlinear analysis of masonry walls. Computers & Structures **88**(3), 135–143 (2010). https://doi.org/10.1016/j.compstruc.2009.08.006
28. Portioli, F.P.A., Godio, M., Calderini, C., Lourenço, P.B.: A variational rigid-block modeling approach to nonlinear elastic and kinematic analysis of failure mechanisms in historic masonry structures subjected to lateral loads. Earthquake Engineering & Structural Dynamics **50**(12), 3332–3354 (2021). https://doi.org/10.1002/eqe.3512
29. Casapulla, C., Maione, A.: Modelling the dry-contact interface of rigid blocks under torsion and combined loadings: Concavity vs. convexity formulation. International Journal of Non-Linear Mechanics **99**, 86–96 (2018)
30. Yang, D., He, Q.-C.: Micromechanical estimation of the effective wear of elastoplastic fiber-reinforced composites. International Journal of Non-Linear Mechanics **108**, 11–19 (2019)
31. Yadav, O.P., Vyas, N.S.: Stick-slips and jerks in an sdof system with dry friction and clearance. International Journal of Non-Linear Mechanics **137**, 103790 (2021)
32. Chen, Y., Wang, S., Tan, H., Xu, J., He, Y., Wang, S.: Study on the tribological performance at the interface between a steel wire rope and groove during a twisting process. International Journal of Non-Linear Mechanics **166**, 104829 (2024)
33. Jin, X., Xu, H., Wang, Y., Huang, Z.: Approximately analytical procedure to evaluate random stick-slip vibration of duffing system including dry friction. Journal of Sound and Vibration **443**, 520–536 (2019)
34. Calvi, P.M., Calvi, G.M.: Historical development of friction-based seismic isolation systems. Soil Dynamics and Earthquake Engineering **106**, 14–30 (2018)
35. Mjöberg, B.: Hip prosthetic loosening and periprosthetic osteolysis: A commentary. World journal of orthopedics **13**(6), 574 (2022)
36. Singh, J., Chauhan, A.: A review on sliding wear behaviour of aluminium matrix composites with hybrid reinforcements for automotive applications. Tribology online **9**(3), 121–134 (2014)
37. Ouyang, H., Mottershead, J., Cartmell, M., Brookfield, D.: Friction-induced vibration of an elastic slider on a vibrating disc. International Journal of Mechanical Sciences **41**(3), 325–336 (1999)
38. Hima, N., D'Annibale, F., Dal Corso, F.: Non-smooth dynamics of buckling based metainterfaces: Rocking-like motion and bifurcations. International Journal of Mechanical Sciences **242**, 108005 (2023)
39. Jean, M.: The non-smooth contact dynamics method. Computer methods in applied mechanics and engineering **177**(3–4), 235–257 (1999)
40. Charroyer, L., Chiello, O., Sinou, J.-J.: Self-excited vibrations of a non-smooth contact dynamical system with planar friction based on the shooting method. International Journal of Mechanical Sciences **144**, 90–101 (2018)
41. Kasinos, S., Salsa, R., Palmeri, A.: Dynamic analysis of piecewise linear multi-degree-of-freedom systems subjected to arbitrary general loads. Journal of Sound and Vibration **570**, 117995 (2024)
42. Popov, V.L., et al.: Contact Mechanics and Friction. Springer, Berlin, Heidelberg (2010)
43. Williams, J.A.: Wear and wear particles–some fundamentals. Tribology international **38**(10), 863–870 (2005)
44. Maeda, K., Bismarck, A., Briscoe, B.: Mechanisms of scratching frictions and damage maps for rubber compounds. Wear **259**(1–6), 651–660 (2005)
45. Shillor, M., Sofonea, M., Telega, J.J.: Models and Analysis of Quasistatic Contact: Variational Methods, vol. 655. Springer, New York (2004)
46. Wriggers, P.: Computational contact mechanics. Computational Mechanics **49**(6), 685 (2012)
47. Lemaitre, J., Desmorat, R.: Engineering Damage Mechanics: Ductile, Creep. Fatigue and Brittle Failures. Springer, Berlin, Heidelberg (2006)
48. Caughey, T.: Sinusoidal excitation of a system with bilinear hysteresis. J. Appl. Mech. **27**(4), 640–643 (1960)
49. Masri, S.: Forced vibration of the damped bilinear hysteretic oscillator. The Journal of the Acoustical Society of America **57**(1), 106–112 (1975)
50. Challamel, N., Gilles, G.: Stability and dynamics of a harmonically excited elastic-perfectly plastic oscillator. Journal of Sound and Vibration **301**(3–5), 608–634 (2007)
51. Capecchi, D., Vestroni, F.: Asymptotic response of a two dof elastoplastic system under harmonic excitation. internal resonance case. Nonlinear Dynamics **7**, 317–333 (1995)
52. Okuizumi, N., Kimura, K.: Multiple time scale analysis of hysteretic systems subjected to harmonic excitation. Journal of Sound and Vibration **272**(3–5), 675–701 (2004)
53. Casalotti, A., Lacarbonara, W.: Nonlinear vibration absorber optimal design via asymptotic approach. Procedia IUTAM **19**, 65–74 (2016)

54. Williamson, E.B., Hjelmstad, K.D.: Nonlinear dynamics of a harmonically-excited inelastic inverted pendulum. Journal of engineering mechanics **127**(1), 52–57 (2001)
55. An, Y., Xue, Z., Ou, J.: Deep learning-based sparsity-free compressive sensing method for high accuracy structural vibration response reconstruction. Mechanical Systems and Signal Processing **211**, 111168 (2024). https://doi.org/10.1016/j.ymssp.2024.111168
56. Patil, S., Banerjee, S., Tallur, S.: Smart structural health monitoring (shm) system for on-board localization of defects in pipes using torsional ultrasonic guided waves. Scientific Reports **14**(1), (2024) https://doi.org/10.1038/s41598-024-76236-w
57. Mishra, M., Barman, T., Ramana, G.V.: Artificial intelligence-based visual inspection system for structural health monitoring of cultural heritage. Journal of Civil Structural Health Monitoring **14**(1), 103–120 (2024). https://doi.org/10.1007/s13349-022-00643-8
58. Scalet, G., Auricchio, F.: Computational methods for elastoplasticity: An overview of conventional and less-conventional approaches. Archives of Computational Methods in Engineering **25**(3), 545–589 (2018). https://doi.org/10.1007/s11831-016-9208-x
59. Simo, J.C., Hughes, T.J.R.: Computational Inelasticity. Springer, New York, NY (1998). https://doi.org/10.1007/b98904
60. Formica, G., Lacarbonara, W.: Three-dimensional modeling of interfacial stick-slip in carbon nanotube nanocomposites. International Journal of Plasticity **88**, 204–217 (2017). https://doi.org/10.1016/j.ijplas.2016.10.012
61. Formica, G., Milicchio, F., Lacarbonara, W.: Computational efficiency and accuracy of sequential nonlinear cyclic analysis of carbon nanotube nanocomposites. Advances in Engineering Software **125**, 126–135 (2018). https://doi.org/10.1016/j.advengsoft.2018.08.013
62. Formica, G., Milicchio, F., Lacarbonara, W.: Hysteretic damping optimization in carbon nanotube nanocomposites. Composite Structures **194**, 633–642 (2018). https://doi.org/10.1016/j.compstruct.2018.04.027
63. Ravichandran, N., Losanno, D., Parisi, F.: Comparative assessment of finite element macro-modelling approaches for seismic analysis of non-engineered masonry constructions. Bulletin of Earthquake Engineering **19**, 5565–5607 (2021)
64. D'Annibale, F., Luongo, A.: A damage constitutive model for sliding friction coupled to wear. Continuum Mechanics and Thermodynamics **25**, 503–522 (2012)
65. D'Annibale, F., Casalotti, A., Luongo, A.: Stick-slip and wear phenomena at the contact interface between an elastic beam and a rigid substrate. Mathematics and Mechanics of Solids **26**(6), 843–860 (2021)
66. Ortiz, M., C, S.J.: An analysis of a new class of integration algorithms for elastoplastic constitutive relations. International Journal for Numerical Methods in Engineering **23**(3), 353–366 (1986) https://doi.org/10.1002/nme.1620230303
67. Hiley, R.A., Rouainia, M.: Explicit runge-kutta methods for the integration of rate-type constitutive equations. Computational Mechanics **42**, 53–66 (2008). https://doi.org/10.1007/s00466-007-0234-2
68. Press, W.H., Teukolsky, S.A., Vetterling, W.T., Flannery, B.P.: Numerical Recipes: The Art of Scientific Computing, 3rd edn. Cambridge University Press, Cambridge (2007). Chap. 17.1 Runge-Kutta Method
69. Butcher, J.C.: Numerical Methods for Ordinary Differential Equations, 3rd edn. John Wiley & Sons, Ltd, New York (2016). https://doi.org/10.1002/9781119121534
70. Casalotti, A., D'Annibale, F.: On the nonlinear dynamics of in-contact rigid bodies experiencing stick-slip and wear phenomena. Continuum Mechanics and Thermodynamics **36**, 1815–1831 (2024)
71. Chiaraluce, L., Chiarabba, C., De Gori, P., Di Stefano, R., Improta, L., Piccinini, D., Schlagenhauf, A., Traversa, P., Valoroso, L., Voisin, C.: The 2009 L'Aquila (central Italy) seismic sequence. Bollettino di Geofisica Teorica ed Applicata (2011)
72. Bradley, B.A.: Correlation of arias intensity with amplitude, duration and cumulative intensity measures. Soil Dynamics and Earthquake Engineering **78**, 89–98 (2015)